

Molten Salt Synthesis of Disordered Spinel $\text{LiNi}_{0.5}\text{Mn}_{1.5}\text{O}_4$ with Improved Electrochemical Performance for Li-ion Batteries

Nabilah Mokhtar¹, Nurul Hayati Idris^{1,} and M.F. Md Din²*

¹ School of Ocean Engineering, Universiti Malaysia Terengganu, 21030 Kuala Nerus, Terengganu, Malaysia.

² Department of Electrical & Electronic Engineering, Faculty of Engineering, National Defence University of Malaysia, Kem Sungai Besi, 57000 Kuala Lumpur, Malaysia.

*E-mail: nurulhayati@umt.edu.my

Received: 5 July 2018 / Accepted: 3 September 2018 / Published: 1 October 2018

Disordered spinel $\text{LiNi}_{0.5}\text{Mn}_{1.5}\text{O}_4$ (LNMO) was successfully synthesised via a molten-salt method using a mixture of $\text{LiOH}\cdot\text{H}_2\text{O}$ and LiNO_3 salts. The precursor was annealed at 750, 850 or 950 °C for 12 h, and the effects of calcination temperature on the structure, morphology and electrochemical performance of the resultant LNMO were investigated. At 850 °C, LNMO exhibited a polyhedral shape approximately 0.75 μm in size with a specific surface area of 1.8135 $\text{m}^2 \text{g}^{-1}$. Electrochemical results indicated that, among the samples tested, the LNMO sample annealed at 850 °C exhibited the highest discharge capacity of 122 mAh g^{-1} at the 1st cycle; these samples also retained 97% of its capacity after 80 rounds of cycling at a rate of 0.2 C. The same sample showed excellent rate capability, indicating exceptional performance even at a high current density. The improved performance of the resulting electrode could be attributed to the homogeneity and small size of the LNMO particles; these characteristics help facilitate Li-ion transport by reducing the Li-ion pathway within the electrode material.

Keywords: Lithium-ion batteries; cathode; $\text{LiNi}_{0.5}\text{Mn}_{1.5}\text{O}_4$; discharge capacity; rate capability.

1. INTRODUCTION

The demands of lithium-ion (Li-ion) batteries for portable electronic devices have increased annually since its introduction to the market on 1991. However, the power density of Li-ion batteries is far too low for large applications, such as electric and hybrid electric vehicles, because extensive polarisation occurs at high current densities [1]. LiCoO_2 [2-4], LiMn_2O_4 [5-7], LiFePO_4 [8-10] and LiNiO_2 [11-13] are among the earliest cathode materials studied to date. Although LiCoO_2 and LiNiO_2 show high discharge capacity and excellent reversibility, these materials are expensive and toxic. By comparison, LiMn_2O_4 is much safer and less expensive; unfortunately, its capacity fades quickly as a

result of the destruction of the material structure caused by Mn^{3+} dissolution [14-16]. Elemental substitution by substituting transition metals into Mn sites in the spinel has been shown to improve the structural stability of cathode materials [17-19]. In particular, $\text{LiNi}_{0.5}\text{Mn}_{1.5}\text{O}_4$ (LNMO) has sparked great research interest for its remarkable properties, which include a high operating voltage (~ 4.7 V), high theoretical capacity (~ 147 mAh g^{-1}) and high energy density (~ 658 Wh kg^{-1}) [20, 21].

LNMO presents two types of structures: the ordered structure (space group, $P4_332$) and the disordered structure (space group, $Fd3m$). These structures form depending on the annealing temperature applied during synthesis. LNMO with a space group of $P4_332$ can be obtained at annealing temperatures less than 700 °C while LNMO with a space group of $Fd3m$ is obtained at higher annealing temperatures (≥ 850 °C) [22, 23]. Although the disordered structure of LNMO has shown better electrochemical performance than its ordered structure because the former presents an adequate amount of Mn^{3+} [24], in general, the performance of both structures may be less than optimal since synthesising pure-phase LNMO is difficult. The presence of impurities, such as NiO and $\text{Li}_{1-x}\text{Ni}_x\text{O}$ [25-27], adds defects to the LNMO spinel structure and thus, reduces the electrochemical performance of the material [25]. To eliminate secondary LNMO phases from forming, various synthesis methods, such as the sol-gel method [28], the emulsion drying method [25], carbon combustion [29] and spray pyrolysis [30], have been reported. Despite their advantages, however, all of these methods present high costs and complicated synthetic routes [31].

Application of molten salt is a promising method used to prepare ultrafine powders for mass production. By using salt with a low melting point, such as hydroxides, sulphates and carbonates, as a reaction medium [31], the particle structure and morphology of the resultant products can be controlled since the salt melt allows higher diffusion rates between ions and improves dissolution to promote the crystallisation process [32, 33]. Molten salts have been widely used to synthesise various cathode materials, including $\text{LiNi}_{0.5}\text{Co}_{0.5}\text{O}_2$ [34], $\text{LiNi}_{1/3}\text{Co}_{1/3}\text{Mn}_{1/3}\text{O}_2$ [35], LiCoO_2 [36] and LiFePO_4 [37]. Kim et al. [31] systematically studied the effect of synthetic parameters such as time, temperature and atmosphere during LNMO synthesis by using a mixture of LiOH and LiCl as the molten medium. The LNMO obtained was spherical in shape and could afford high tap-density particles, leading to improvements in energy density in the final battery [38]. In another report, the use of NaCl and KCl as molten salts was intensively investigated [39]. The results showed discharge capacities of approximately 129 mAh g^{-1} at the 1st cycle and 127 mAh g^{-1} at the 50th cycle.

In the present study, LNMO was synthesised via the molten salt method with $\text{LiOH}\cdot\text{H}_2\text{O}$ and LiNO_3 and the electrochemical performance of the cathode material produced was investigated. Marzuki et al. [33] showed that a porous Co_3O_4 structure could be obtained by utilising $\text{LiOH}\cdot\text{H}_2\text{O}$ and LiNO_3 as the molten medium. Particle homogeneity and a large surface area appeared to enhance the electrochemical performance of the LNMO obtained.

2. METHODOLOGY

2.1 Preparation of $\text{LiNi}_{0.5}\text{Mn}_{1.5}\text{O}_4$ powders

LNMO powders were prepared by mixing MnCO_3 (Aldrich), $\text{C}_2\text{H}_6\text{Ni}_5\text{O}_{12}\cdot 4\text{H}_2\text{O}$ (Aldrich, 99%), LiNO_3 (Sigma-Aldrich), $\text{LiOH}\cdot\text{H}_2\text{O}$ (Sigma-Aldrich, 99%) and H_2O_2 (Merck Schuchardt, 30%) and grinded using an agate mortar to form a homogeneous mixture. The precursor was transferred to an alumina crucible and heated at 120 °C for 8 h under vacuum. Afterward, the LNMO precursor was annealed first at 400 °C for 4 h and then at 750, 850 or 950 °C for 12 h in air. Finally, the powders were washed several times using deionised water and ethanol and dried at 100 °C for 6 h under vacuum. The obtained powders are marked M750, M850 and M950 according to their post-annealing temperature.

2.2 Characterisation of $\text{LiNi}_{0.5}\text{Mn}_{1.5}\text{O}_4$ powders

The structure of the LNMO powders was determined by X-ray diffractometry (XRD) (Rigaku Miniflex II) with $\text{Cu K}\alpha$ radiation at wavelength of 1.5418 Å. XRD was performed over the 2θ range of 5°–80° at a scan rate of 0.2° min^{-1} . Rietveld refinement was carried out using Fullprof software (version 5.60). The morphology of the LNMO powders was characterised by scanning electron microscopy (SEM; JEOL JSM-6360LA) and transmission electron microscopy (TEM; JEOL JEM-2100F). The specific surface area of the samples was determined via the Brunauer–Emmett–Teller (BET) method using a surface area analyser (Micromeritics ASAP 2020). To prepare the electrode, 75 wt.% LNMO, 20 wt.% carbon black and 5 wt.% carboxymethyl cellulose (CMC) (Sigma-Aldrich) were dissolved in deionised water, pasted onto aluminium foil over a geometrical area of $1 \times 1 \text{ cm}^2$ and dried at 100 °C under vacuum. The weight of the active material obtained was about 1–2 mg. The cell was assembled with lithium metal as the counter electrode and polypropylene film as the separator in an argon-filled glove-box, and the electrolyte used was 1 M LiPF_6 in a mixture of ethylene carbonate and dimethyl carbonate (1:1 by volume). Galvanostatic charging-/discharging was performed at a voltage range of 3.0–4.9 V, and cyclic voltammetry (CV) was conducted using CH Instruments equipment (CHI760e) at a scan rate of 0.5 mV s^{-1} .

3. RESULTS AND DISCUSSION

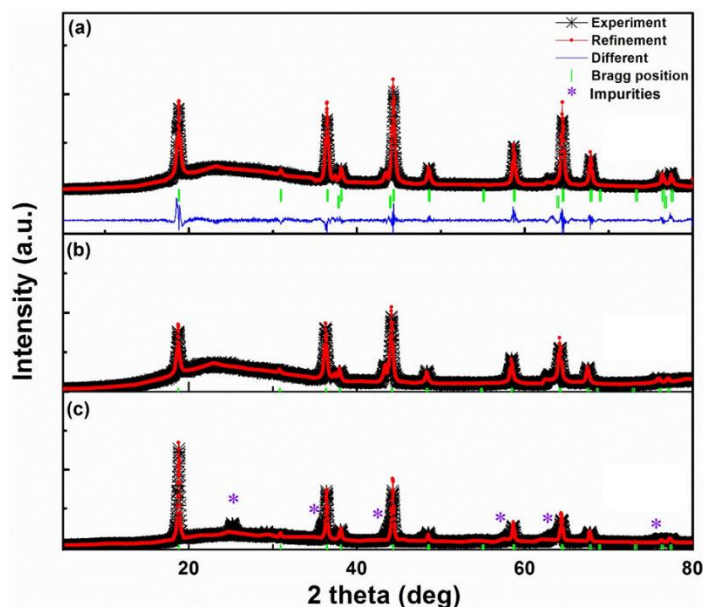


Figure 1. Rietveld refinements of the XRD data of the samples (a) M750 (b) M850 and (c) M950.

The XRD patterns of M750, M850 and M950 are shown in Figure 1. All of the diffraction peaks the powders clearly showed high crystallinity and could be assigned to the cubic spinel structure of the $Fd\bar{3}m$ space group (JCPDS 80-2162). The diffraction peaks of 18.69° , 36.22° , 37.91° , 44.05° , 48.32° , 58.29° , 64.07° , 67.36° , 75.91° and 76.98° could respectively be indexed to the (111), (311), (400), (331), (511), (440), (531), (533), (622), (444) and (551) crystal planes of LNMO. Small impurity peaks at 37.64° , 43.69° , 63.27° , 75.37° and 79.38° indicated the features of NiO (JCPDS 73-1523) and could be detected in all of the samples. The presence of impurities is due to oxygen deficiency during the synthesis process [20, 31] and could reduce the electrochemical performance of the LNMO samples. The crystallite size of the LNMO powders was calculated using Scherer's equation as shown in Equation (1):

$$L = \frac{k\lambda}{\beta \cos \theta} \quad (1)$$

where L is the crystallite size, k is a constant (0.9394), λ is the Cu $K\alpha$ radiation wavelength (1.5148 \AA), β is the full width at half maximum of the major XRD peak in radians and θ is the angle of diffraction. The crystallite sizes of M750, M850 and M950 were found to be 218.51, 138.57 and 164.93 nm, respectively.

Table 1. Rietveld refinements results for the samples M750, M850 and M950.

Sample	Phase	wt%	a (\AA)	Bragg R_{factor} (%)	R_{F} factor (%)	χ^2
M750	LNMO	98.26 (6)	8.1689	8.6	9.5	1.93
	NiO	1.74 (2)	4.1121	26.7	18.4	

M850	LNMO	96.38 (8)	8.1988	9.8	10.3	0.54
	NiO	3.62 (14)	4.1373	7.14	14.3	
M950	LNMO	93.09 (9)	8.2674	18.4	13.6	5.65
	NiO	6.91 (8)	4.1532	6.9	5.4	

Table 1 lists the Rietveld refinement results of the powders; here, the weight fraction of the LNMO phase clearly decreased from 98.26% in M750 to 93.09% in M950. By contrast, the weight fraction of NiO increased from 1.74% in M750 to 3.62% in M850 and 6.91% in M950. The lattice parameters, a , of M750, M850 and M950 are also listed in Table 1; here, a increased with increasing temperature, and values of 8.1689, 8.1980 and 8.2674 Å were obtained for samples M750, M850 and M950, respectively. Increases in a could be attributed to oxygen loss from the lattice with increasing temperature [17]. Oxygen deficiency increases the Mn³⁺ content relative to the Mn⁴⁺ content, which, in turn, increases a [17, 40].

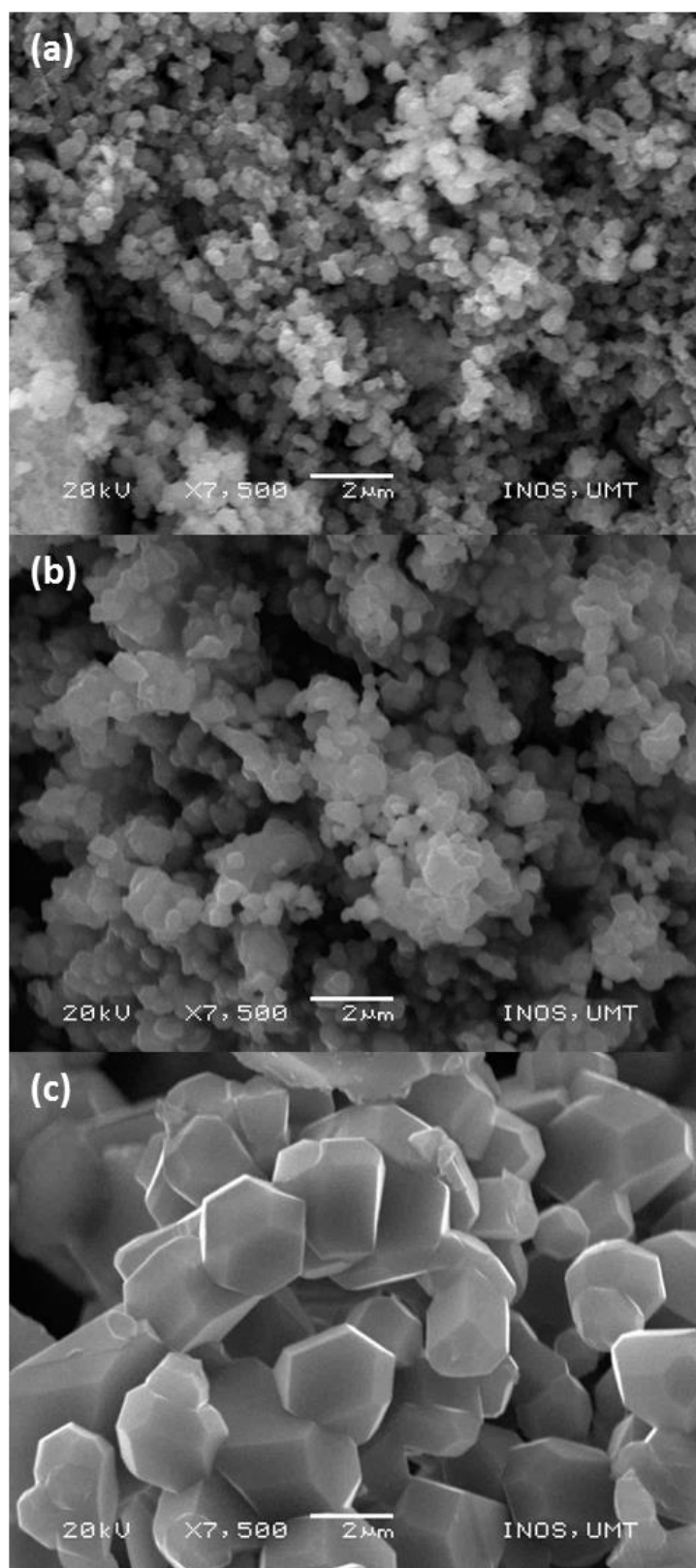


Figure 2. SEM images of samples (a) M750 (b) M850 and (c) M950 after annealed at 750, 850 or 950 °C for 12 h in air.

The morphology of the LNMO powders is shown in Figure 2. As the annealing temperature increased, the particle size of the LNMO powders increased. M750 (Fig. 2a) consisted of nanoparticles of about 0.3 μm size with a homogeneous distribution.

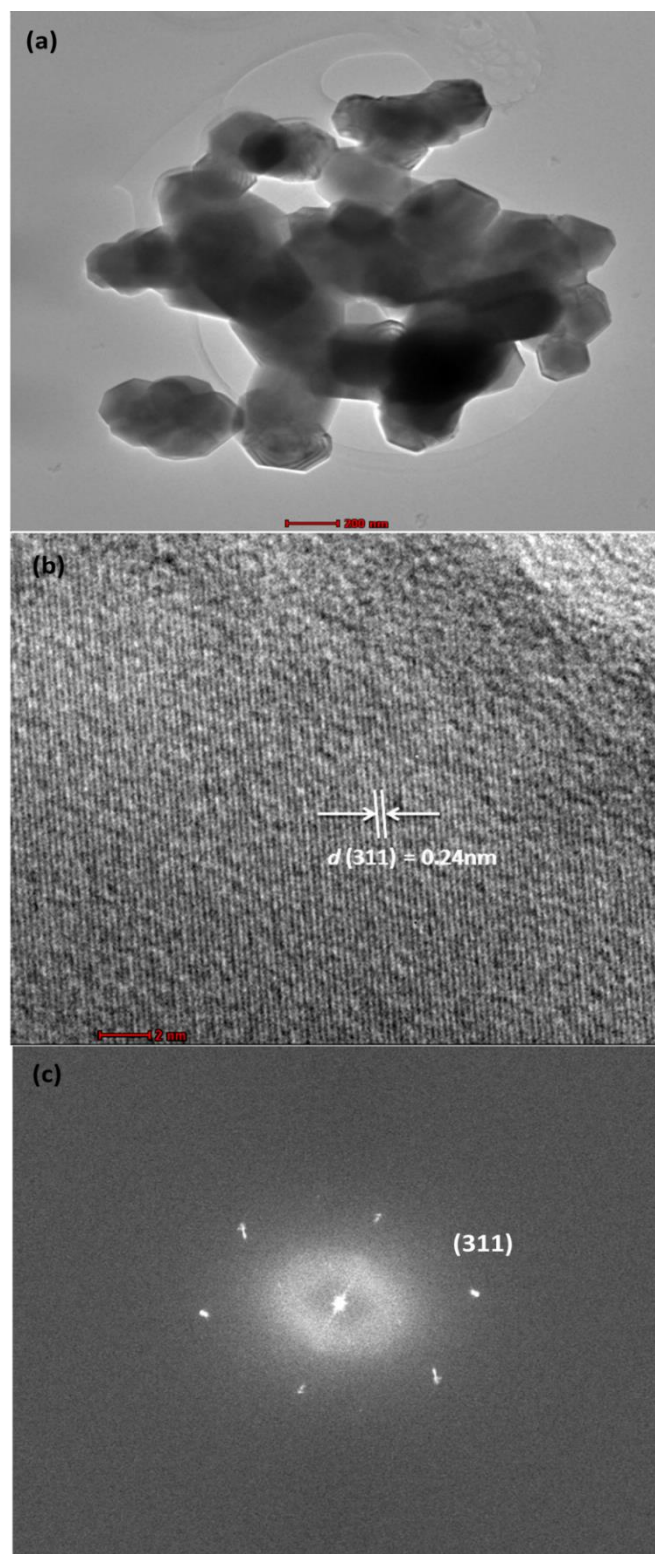


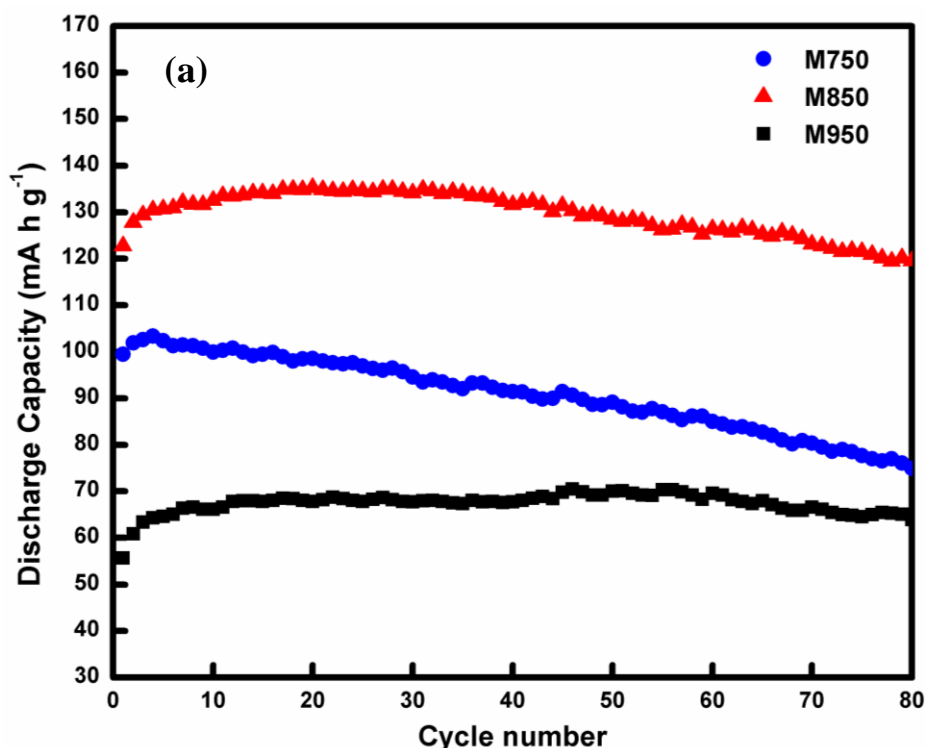
Figure 3. TEM images of sample M850 at (a) low magnification (b) high-resolution TEM and (c) fast Fourier transform.

Particle sizes were increased ($\sim 0.75\ \mu\text{m}$) at $850\ ^\circ\text{C}$ and began to develop a polyhedral shape, as shown in Fig. 2b. M950 formed a well-defined polyhedral with a faceted surface and size of about $2.5\ \mu\text{m}$; this sample showed the highest degree of crystallinity among the samples obtained (Fig. 2c).

The BET test was employed to determine the specific surface area of the LNMO powders. The specific surface areas of M750, M850 and M950 were calculated to be approximately 3.7877, 1.8135 and 1.4834 $\text{m}^2 \text{g}^{-1}$, respectively. These results are consistent with SEM observations indicating that M750 presents the smallest particle sizes and therefore, the largest specific surface area among the powders synthesised. The large particle sizes of M950 yield a small specific surface area that could reduce the Li-ion diffusion path during intercalation/deintercalation; as such, this sample may be expected to show poor rate capability and a low discharge capacity.

The microstructure of M850 was further investigated by TEM (Fig. 3). Figure 3a revealed agglomerates of crystalline LNMO and confirmed the formation of a polyhedral shape; these findings agree well with the SEM images. High-resolution TEM (HRTEM) revealed clear lattice fringes (Fig. 3b), and an interplanar distance of 0.24 nm corresponding to the characteristic (311) plane of LNMO of the $Fd\bar{3}m$ space group was noted [41]. The fast Fourier transform (FFT) pattern of M850 showed the crystalline behaviour of the LNMO powder [41]. Overall, the FFT patterns obtained were consistent with the (311) plane determined by HRTEM and confirm that the samples formed as single crystals [42].

Electrochemical characterisations were conducted to study the performance of the LNMO electrodes when assembled as a cathode in a half-cell. Figure 4a compares the discharge capacities of the M750, M850 and M950 electrodes at a constant rate of 0.2 C. The M850 electrode exhibited the highest discharge capacity, followed by the M750 electrode and then the M950 electrode. At the 1st cycle, the discharge capacity of the M850 electrode was approximately 122 mAh g^{-1} . This discharge capacity then increased to a maximum (135 mAh g^{-1}) at the 20th cycle and slowly decreased thereafter.



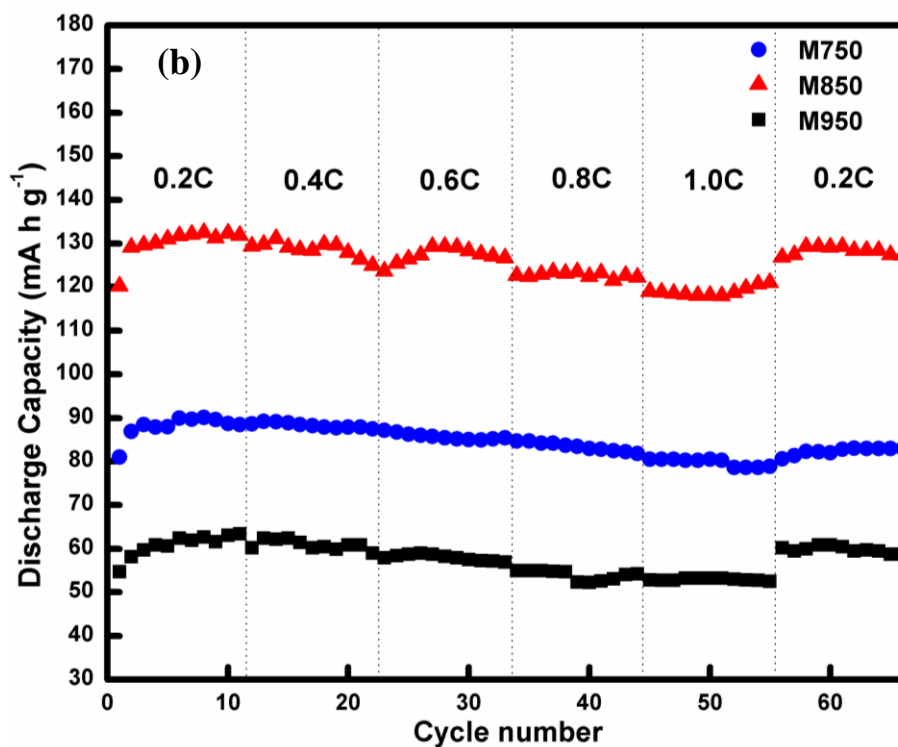


Figure 4. Comparative (a) discharge capacity at 0.2 C for 80 cycles and (b) rate capability of LNMO electrodes.

A similar trend was observed in the M750 and M950 electrodes. After the 80th cycle, the discharge capacities of the M750, M850 and M950 electrodes were only 74, 119 and 63 mAh g⁻¹, respectively.

The high discharge capacity of the M850 electrode could be attributed to the large specific surface area and high crystallinity of the LNMO powder. Although M750 presented the largest specific surface area among the samples studied, this electrode also exhibited the poorest cyclability. Increases in surface area have been reported to promote the dissolution of Ni and Mn ions, causing capacity loss during cycling [43]. M750 exhibited a discharge capacity lower than that of M850, and this poorer performance is caused by instability reactions between the active material and electrolyte resulting from the larger surface area of the M750 powder [44]. M950 presented significant capacity reduction because its large particle size lengthens the Li⁺ diffusion path [43].

The rate capability of the electrodes was investigated at different rates ranging from 0.2 C to 1 C, and the corresponding plot is shown in Fig. 4b. The M850 electrode clearly showed better rate capability performance than the M750 and M950 electrodes. At the 11th cycle, the M850 electrode delivered discharge capacities of 131, 125, 126, 122 and 121 mAh g⁻¹ at rates of 0.2, 0.4, 0.6, 0.8 and 1 C, respectively. When the rate was returned to 0.2 C, the discharge capacity of the electrode recovered to approximately 127 mAh g⁻¹, indicating stable cycling performance. Even at a high rate of 1 C, the electrode could deliver 86% of the theoretical capacity of LNMO (147 mAh g⁻¹). By contrast, the M750 and M950 electrodes showed much lower capacity retention.

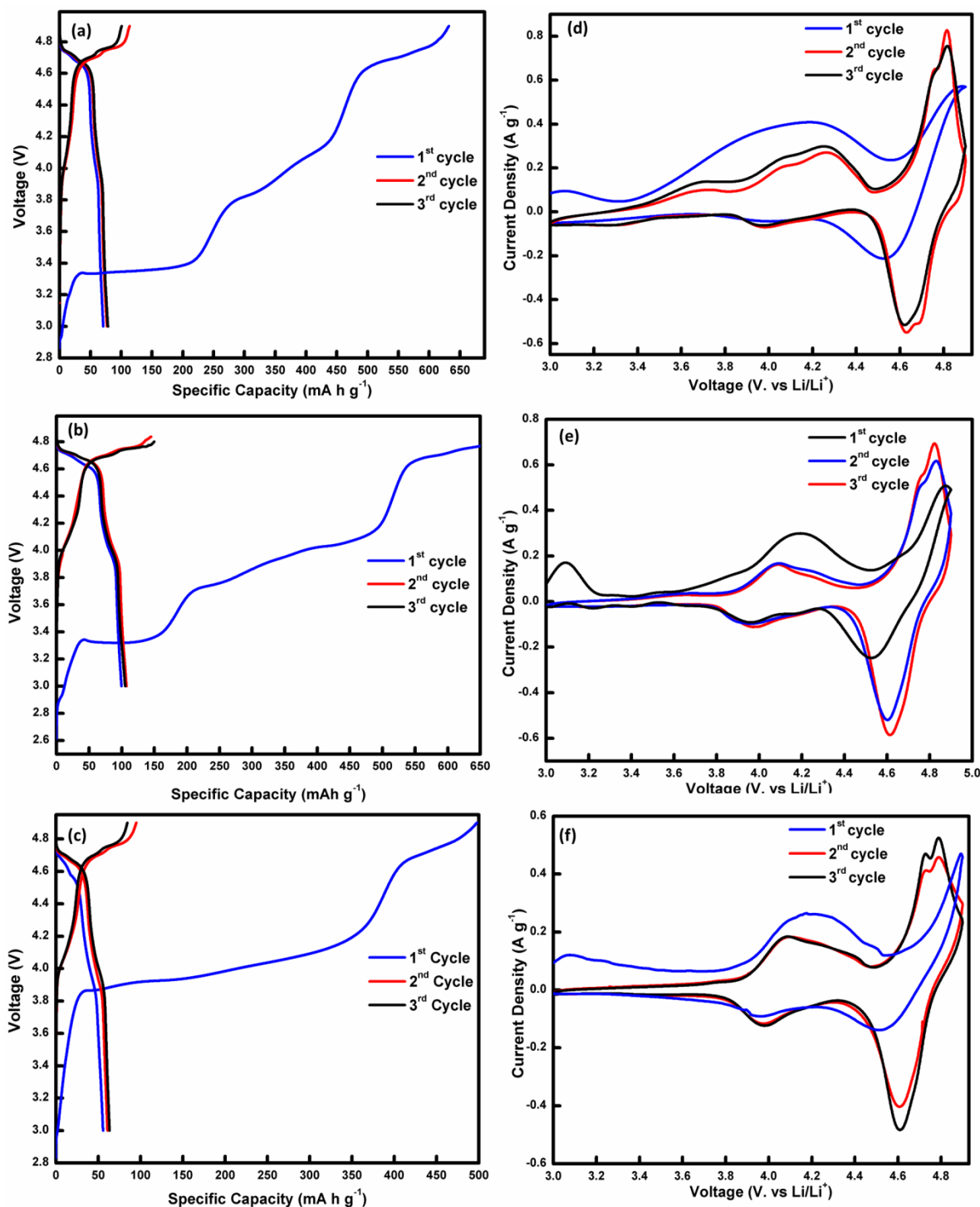
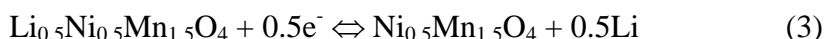


Figure 5. Charge-discharge profiles at 0.2 C for the first 3 cycles and CV curves at a scan rate of 0.5 mV s^{-1} for samples (a, d) M750 (b, e) M850 and (c, f) M950.

Typical charge-discharge profiles are shown in Figs. 5a–5c, and these curves are in good agreement with the CV results (Figs. 5d–5f). All of the discharge curves exhibited a flat voltage plateau at about 4.7 V and a minor plateau at about 4.0 V. Similarly, in the CV curves, a redox peak, which is attributed to the presence of $\text{Mn}^{3+}/\text{Mn}^{4+}$, could be seen at 4.0 V and a major peak, which can

be ascribed to the redox peaks of $\text{Ni}^{2+}/\text{Ni}^{3+}$ and $\text{Ni}^{3+}/\text{Ni}^{4+}$, could be observed at 4.7 V [8]. The reactions corresponding to the 4.7 V peak are as follows:



Considering these equations, the redox reactions of Ni ions at 4.7 V could be a major factor influencing the Li-ion intercalation/deintercalation capacity of LNMO [45]. The minor curves and short plateau at 4 V suggest a low Mn^{3+} content. This result is of great importance because high Mn^{3+} contents cause poor cycling performance resulting from the disproportionate reactions of Mn^{3+} , which cause dissolution of Mn^{2+} into the electrolyte, and the strain arising from the Jahn-Teller distortion of Mn^{3+} . Hence, low Mn^{3+} contents will improve the cycling performance where it reduce the dissolution of Mn^{2+} into the electrolyte [46].

Different annealing temperatures appeared to influence the crystallinity, particle size and morphology of the samples, ultimately affecting the electrochemical performance of the LNMO electrodes. The presence of impurities in the LNMO samples limits their cycling behaviour because impurities can block the Li-ion diffusion path within the materials [40, 47]. The blocked Li-ion diffusion channels could lower the ion diffusion coefficient in the plateau region and thereby, decreases the electrochemical performances of the materials [48, 49]. M850 exhibited excellent discharge capacity, cyclability and rate capability, and these characteristics are attributed to the homogeneity, uniform morphology, small size and high crystallinity of the sample particles, all of which contribute to a large surface area that is beneficial for Li-ion transport during the intercalation/deintercalation process.

Table 2. Previous research on LNMO synthesized using molten salt method.

Molten salt	Annealing temperature and time	Current density (mA g^{-1})	Discharge capacity (mAh g^{-1})/cycle	References
LiOH and LiCl	900 °C for 3 hours	20	139/1 st cycle	[31]
NaCl and KCl	800 °C for 12 hours	130	135/1 st cycle	[39]
LiOH.H ₂ O and LiNO ₃	850 °C for 12 hours	29	122/1 st cycle	This work

M750 exhibited a particle size smaller than that observed in M850, but the particles of this sample presented an irregular surface formation. Moreover, the high surface area of this sample led to its poor cyclability and discharge capacity, probably because of the extensive dissolution of electrolytes over larger surface areas [45]. Optimising capacity in this case may prove to be challenging because electric contact between LNMO and the current collector is reduced by inhibition of surface contact between the electrode and the electrolyte [44, 50].

M950 presented large particle sizes suggestive of a small surface area, which increases the diffusion path of Li-ions and results in poor LNMO electrode performance. The use of the molten salt method is believed to offer important advantages, such as control of the morphology and structure of the resulting LNMO particles, because phase formation is significantly accelerated in the molten media [31, 51]. To the best of the author's knowledge, only two works on the synthesis of LNMO via the molten salt method have been published. The discharge capacity obtained in this work is higher than that reported in the literature, as listed in Table 2. Thus, the present study offers a simple and promising technique to prepare complex oxides and can be extended to the synthesis of other cathode materials.

4. CONCLUSIONS

This work presents the synthesis of LNMO using the molten salt method. The physical and electrochemical characteristics of the LNMO obtained were investigated by XRD, SEM, TEM, BET, CV and galvanostatic charge-discharge tests. NiO formed in the LNMO samples, likely because of oxygen deficiency during annealing at temperatures over 700 °C. Despite its large surface area ($1.8135 \text{ m}^2 \text{ g}^{-1}$) and small particle size ($0.75 \text{ }\mu\text{m}$), M850 exhibited a superior discharge capacity of 119 mAh g^{-1} compared with those of M750 (74 mAh g^{-1}) and M950 (63 mAh g^{-1}) after 80 cycles at 0.2 C. M850 also demonstrated excellent rate capability; these features could be attributed to the high crystallinity, uniform polyhedral morphology, homogeneity and small particle sizes of the material.

ACKNOWLEDGEMENT

Financial support was provided by the Ministry of Higher Education, Malaysia through a Fundamental Research Grant Scheme (FRGS) (Vote no. 59323) and MyBrain15 for the scholarships sponsored to the student is gratefully acknowledged.

References

1. H. Wang, T.A. Tan, P. Yang, M.O. Lai, L. Lu, *J. Phys. Chem. C*, 115 (2011) 6102-6110.
2. J. Geder, H.E. Hoster, A. Jossen, J. Garche, D.Y.W. Yu, *J. Power Sources*, 257 (2014) 286-292.
3. T. Fang, J.-G. Duh, S.-R. Sheen, *Thin Solid Films*, 469-470 (2004) 361-365.
4. N.H. Kwon, *Solid State Sci.*, 21 (2013) 59-65.
5. Y. Cai, Y. Huang, X. Wang, D. Jia, W. Pang, Z. Guo, Y. Du, X. Tang, *J. Power Sources*, 278 (2015) 574-581.
6. L. Xiong, Y. Xu, T. Tao, J. Song, J.B. Goodenough, *J. Mater. Chem.*, 22 (2012) 24563.
7. M.O. Guler, A. Akbulut, T. Cetinkaya, M. Uysal, H. Akbulut, *Int. J. Hydrogen Energy*, 39 (2014)

- 21447-21460.
8. C.-H. Yim, E.A. Baranova, Y. Abu-Lebdeh, I. Davidson, *J. Power Sources*, 205 (2012) 414-419.
 9. D. Zhao, Y.-L. Feng, Y.-G. Wang, Y.-Y. Xia, *Electrochim. Acta*, 88 (2013) 632-638.
 10. W. Chang, S.-J. Kim, I.-T. Park, B.-W. Cho, K.Y. Chung, H.-C. Shin, *J. Alloys Compd.*, 563 (2013) 249-253.
 11. S.N. Kwon, J. Song, D.R. Mumm, *Ceram. Int.*, 37 (2011) 1543-1548.
 12. Y.S. Lee, Y.K. Sun, K.S. Nahm, *Solid State Ionics*, 118 (1999) 159-168.
 13. M.Y. Song, R. Lee, *J. Power Sources*, 111 (2002) 97-103.
 14. M. Jo, Y.-K. Lee, K.M. Kim, J. Cho, *J. Electrochem. Soc.*, 157 (2010) A841-A845.
 15. Y. Xia, M. Yoshio, *J. Electrochem. Soc.*, 143 (1996) 825-833.
 16. R.J. Gummow, A.d. Kock, M.M. Thackeray, *Solid State Ionics*, 69 (1994) 59-67.
 17. M.V. Reddy, S.S. Manoharan, J. John, B. Singh, G.V. Subba Rao, B.V.R. Chowdari, *J. Electrochem. Soc.*, 156 (2009) A652-A660.
 18. J. Breger, Y.S. Meng, Y. Hinuma, S. Kumar, K. Kang, Y. Shao-Horn, G. Ceder, C.P. Grey, *Chem. Mater.*, 18 (2006) 4768-4781.
 19. S.-K. Jung, H. Gwon, J. Hong, K.-Y. Park, D.-H. Seo, H. Kim, J. Hyun, W. Yang, K. Kang, *Adv. Energy Mater.*, 4 (2014) 1300787.
 20. Y.-Z. Lv, Y.-Z. Jin, Y. Xue, J. Wu, X.-G. Zhang, Z.-B. Wang, *RSC Adv.*, 4 (2014) 26022-26029.
 21. J. Ma, P. Hu, G. Cui, L. Chen, *Chem. Mater.*, 28 (2016) 3578-3606.
 22. D. Li, A. Ito, K. Kobayakawa, H. Noguchi, Y. Sato, *Electrochim. Acta*, 52 (2007) 1919-1924.
 23. J. Yoon, D. Kim, J.H. Um, M. Jeong, W. Oh, W.-S. Yoon, *J. Alloys Compd.*, 686 (2016) 593-600.
 24. G. Liun, X. Kong, H. Sun, B. Wang, *Ceram. Int.*, 40 (2014) 14391-14395.
 25. S.-T. Myung, S. Komaba, N. Kumagai, H. Yashiro, H.-T. Chung, T.-H. Cho, *Electrochim. Acta*, 47 (2002) 2543-2549.
 26. Q. Zhong, A. Bonakclarpour, M. Zhang, Y. Gao, J.R. Da, *J. Electrochem. Soc.*, 144 (1997) 205-213.
 27. K. Amine, H. Tukamoto, H. Yasuda, Y. Fuiita, *J. Electrochem. Soc.*, 143 (1996) 1607-1613.
 28. R. Santhanam, B. Rambabu, *J. Power Sources*, 195 (2010) 5442-5451.
 29. L. Zhang, X. Lv, Y. Wen, F. Wang, H. Su, *J. Alloys Compd.*, 480 (2009) 802-805.
 30. E.B. Jo, S.H. Ju, H.C. Jang, Y.C. Kang, *J. Ceram. Process. Res.*, 8 (2007) 352-355.
 31. J.H. Kim, S.T. Myung, Y.K. Sun, *Electrochim. Acta*, 49 (2004) 219-227.
 32. J.-F. Ni, H.-H. Zhou, J.-T. Chen, X.-X. Zhang, *Mater. Lett.*, 61 (2007) 1260-1264.
 33. N.S. Marzuki, N.U. Taib, M.F. Hassan, N.H. Idris, *Electrochim. Acta*, 182 (2015) 452-457.
 34. M.V. Reddy, G.V.S. Rao, B.V.R. Chowdari, *J. Phys. Chem. C*, 111 (2007) 11712-11720.
 35. H. Zhu, J. Li, Z. Chen, Q. Li, T. Xie, L. Li, Y. Lai, *Synth. Met.*, 187 (2014) 123-129.
 36. K.S. Tan, M.V. Reddy, G.V.S. Rao, B.V.R. Chowdari, *J. Power Sources*, 147 (2005) 241-248.
 37. C. Zhao-yong, Z. Wei, Z. Hua-li, Z. Jian-li, L. Qi-feng, *Trans. Nonferrous Met. Soc. China*, 20 (2010) 809-813.
 38. X.M. He, J.J. Li, Y. Cai, Y. Wang, J. Ying, C. Jiang, C. Wan, *J. Solid State Electrochem.*, 9 (2005) 438-444.
 39. L. Wen, Q. Lu, G. Xu, *Electrochim. Acta*, 51 (2006) 4388-4392.
 40. E. Zhao, L. Wei, Y. Guo, Y. Xu, W. Yan, D. Sun, Y. Jin, *J. Alloys Compd.*, 695 (2017) 3393-3401.
 41. C. Liu, Z. Wang, C. Shi, E. Liu, C. He, N. Zhao, *ACS Appl. Mater. Interfaces*, 6 (2014) 8363-8368.
 42. S.R. Plissard, I. van Weperen, D. Car, M.A. Verheijen, G.W.G. Immink, J. Kammhuber, L.J. Cornelissen, D.B. Szombati, A. Geresdi, S.M. Frolov, L.P. Kouwenhoven, E.P.A.M. Bakkers, *Nat Nano*, 8 (2013) 859-864.
 43. X. Fang, Y. Lu, N. Ding, X.Y. Feng, C. Liu, C.H. Chen, *Electrochim. Acta*, 55 (2010) 832-837.
 44. N.D. Rosedhi, N.H. Idris, M.M. Rahman, M.F.M. Din, J. Wang, *Electrochim. Acta*, 206 (2016) 374-380.
 45. H.B. Lin, Y.M. Zhang, J.N. Hu, Y.T. Wang, L.D. Xing, M.Q. Xu, X.P. Li, W.S. Li, *J. Power*

Sources, 257 (2014) 37-44.

46. Y. Xue, Z. Wang, F. Yu, Y. Zhang, G. Yin, *J. Mater. Chem. A*, 2 (2014) 4185-4191.
47. Y. Hu, H. Zhao, X. Liu, *Materials*, 11 (2018) 1176.
48. B. Xu, D. Qian, Z. Wang, Y.S. Meng, *Mater. Sci. Eng., R*, 73 (2012) 51-65.
49. R. Malik, D. Burch, M. Bazant, G. Ceder, *Nano Lett.*, 10 (2010) 4123-4127.
50. A.S. Arico, P. Bruce, B. Scrosati, J.-M. Tarascon, W. van Schalkwijk, *Nat. Mater.*, 4 (2005) 366-377.
51. P. Afanasiev, C. Geantet, *Coord. Chem. Rev.*, 178–180, Part 2 (1998) 1725-1752.

© 2018 The Authors. Published by ESG (www.electrochemsci.org). This article is an open access article distributed under the terms and conditions of the Creative Commons Attribution license (<http://creativecommons.org/licenses/by/4.0/>).